FUNDAMENTALS & APPLICATIONS

CHEMELECTROCHEM

ANALYSIS & CATALYSIS, BIO & NANO, ENERGY & MORE

Accepted Article

Title: Tailored Hollow Core/Mesoporous Shell Carbon Nanofibers as Highly Efficient and Durable Cathode Catalyst Supports for Polymer Electrolyte Fuel Cells

Authors: Karthikeyan K Karuppanan, Appu V Raghu, Manoj Kumar Panthalingal, and Biji Pullithadathil

To be cited as: *ChemElectroChem* 10.1002/celc.201900065

Link to VoR: http://dx.doi.org/10.1002/celc.201900065

A Journal of

ChemPubSoc Europe

WILEY-VCH

www.chemelectrochem.org

Tailored Hollow Core/Mesoporous Shell Carbon Nanofibers as Highly Efficient and Durable Cathode Catalyst Supports for Polymer Electrolyte Fuel Cells.

Karthikeyan K Karuppanan,[a] Appu V Raghu[a], Manoj Kumar Panthalingal[b] and Biji Pullithadathil*[a,c]

Abstract: Hierarchical mesoporous hollow carbon nanofibers based electrocatalyst support material has been developed by co-axial electrospinning and deployed for fabrication of PEM Fuel cells. The synergistic effect of high specific surface area (780 m^2/g), homogeneous formation of mesopores (20-50 nm) and hollow nanochannels in the carbon nanofiber matrix lead to uniform distribution of Pt electrocatalysts. XPS analysis revealed the presence of nitrogen species in mesoporous hollow carbon nanofibers in the form of pyridinic, pyrrolic and quaternary nitrogen atoms played a crucial role in the augmentation of triple phase boundaries. Pt/*m*PHCNFs exhibited superior electrocatalytic activity towards ORR with positively shifted onset potential (62 mV), half-wave potential (86 mV) and high limiting current density (4.76 mA/cm^2) compared to commercial electrocatalysts. The Pt/*m*PHCNFs exhibited excellent stability under acidic medium and showed only 23 mV loss in the half-wave potential; whereas, the Pt/CNFs (35 mV) and Pt/C (77 mV) exhibited much higher shift in half-wave potential. The PEM fuel cell testing of Pt/*m*PHCNFs (411 mW/cm^2) based membrane electrode assembly revealed the superior performance compared to Pt/CNFs (297.4 mW/cm^2) and Pt/C (212.8 mW/cm^2). This method can be an effective strategy for the development of durable, low-cost and high-performance polymer electrolyte membrane fuel cells.

Introduction

Polymer electrolyte membrane fuel cells (PEMFCs) represent an outstanding clean energy technology for next generation power sources due to highly desirable characteristics, such as high power density, zero pollution by-product emission, relatively low operating temperature and minimal corrosion issues[1–4]. However, the performance of these devices depends on the physical and chemical properties of the electrocatalyst materials. Pt and its alloys have been extensively used as most efficient electrocatalyst for oxygen reduction reaction (ORR), but high cost and less abundance of Pt still remains as serious problem to the widespread commercialization of fuel cell technologies[5,6]. More specifically, support materials play an indispensable role to modulate the properties of electrocatalyst nanoparticles such as size, shape and distribution which greatly determine the fuel cell performances. An ideal electrocatalyst support materials should possess high electronic conductivity, large surface area, surface reactivity for metal particle dispersion, suitable hierarchical pore structures for the accessibility of reactant and ionomer and electrochemical stability for the effective augmentation of active sites, so-called triple-phase boundaries[7–9]. Carbon blacks are the most prevalently used as the support materials for Pt electrocatalysts, but they are not stable enough to prevent carbon corrosion. During high voltage, acidic and oxidation environmental conditions of PEMFC, the undesirable corrosion properties of carbon blacks may induce the conglomeration or detachment of Pt nanocatalysts[10–12]. Moreover, the presence of tiny micropores in the conventional carbon support is prone to trap the Pt nanoparticles which eventually affect the contact between Nafion ionomer, reactant and catalyst particles that are leading to the loss of triple phase boundary sites[13–16]. The triple phase boundary sites (regions where catalyst particles in the electrically conducting support material, ionomer and gas pores are connected each other) existing in the catalyst layer play a vital role in the performance enhancement of the electrochemical reaction[17–19]. Therefore, the development of an ideal cathode support material with enhanced ORR activity and durability is highly desired for the implementation of PEMFCs for real-time applications. Since then, considerable efforts have been attempted to explore some of the novel nanostructured carbonaceous support materials including carbon nanotubes (CNTs), carbon nanofibers (CNFs), graphene, carbon aerogels, ordered mesoporous carbons (OMCs), hollow graphitic nanoparticles, graphitic carbon nitride and boron-doped diamond (BDD) to improve the electrochemical activity and/or durability[20–27]. Among these numerous carbon support materials, electrospun carbon nanofibers have been fascinated as an indispensable candidate due to their distinguished physicochemical properties owing to their unique nanoscale graphite-like structures demonstrate outstanding electrical conductivity, 1-D structure, high mechanical strength, thermal stability and chemical inertness[21,28,29]. However, significant quantity of electrocatalyst particles can be partially embedded in the micropores of carbon nanofibers making them inaccessible to the ionomer molecules. This reduces the number of triple phase boundary sites leading to the loss of Pt utilization. Meanwhile, the electrochemical performance of carbon nanofibers can be improved by the introduction of porous structure that can eventually facilitate the uniform dispersion of catalyst nanoparticles, charge transfer at electrode-electrolyte interface and efficient mass transport due to their high surface area, high pore volume, adjustable pore sizes, and good electrical conductivity, resulting in excellent electrocatalytic activity[30–34]. The mesoporous network in the support material have strong influence on high specific surface area, optimal pore size (2-50 nm) and large pore volumes that can contribute in the enhancement of electrocatalyst particle distribution, mass transport and ionomer contact[4,8,15,35,36]. Generally, two major methods have been adopted for preparing electrospun porous carbon nanofibers i.e., sacrificial component methods and

[a] Nanosensor Laboratory, PSG Institute of Advanced Studies, Coimbatore-641004, INDIA
E-mail: bijuja123@yahoo.co.in, pbm@psgias.ac.in
[b] Department of Mechanical Engineering, PSG Institute of Technology and Applied Research, Coimbatore- 641 062, INDIA
[c] Department of Chemistry, PSG College of Technology, Coimbathore-641004, INDIA

activation methods. Thermally induced selective phase separation method is widely recognized as a suitable method for preparing porous structure and the commonly used porogens are hard template, soluble salts or, sacrificial polymers[30,31,34,37–39]. Therefore, it is highly desirable to design and fabricate hollow carbon nanofibers tailored with numerous regular mesopores for achieving high-performance electrodes to be used in fuel cells. Recently, poly (acrylonitrile) (PAN) and the coaxial electrospinning process have been frequently employed for development of hollow carbonaceous materials[40–43]. To the best of our knowledge, no attention has been given towards the preparation of mesoporous hollow carbon nanofiber support material based on coaxial electrospinning method especially for oxygen reduction reaction in PEM fuel cells.

Herein, we report a rational method for the preparation of mesoporous hollow carbon nanofibers supported with monodispersed Pt nanoparticles (Pt@*m*PHCNFs) with enhanced TPB sites for oxygen reduction reaction for the fabrication of highly efficient and durable PEM fuel cells. A simple co-axial electrospinning method utilizing a sacrificial core (PMMA) inside carbon shell (PAN) feed solutions followed by thermally induced selective phase separation method was adopted to prepare mesoporous hollow carbon nanofibers support. Induced mesoporosity was achieved in the hollow carbon nanofiber shell by integrating the pore forming agent, $NaHCO_3$ nanoparticles in the PAN nanofiber structure. The mesoporous hollow carbon nanofibers based electrocatalyst support material possessed high specific surface area and pore volume with homogeneous mesopores. More importantly, the nitrogen was found to be doped in carbon lattice which existed in the form of pyridinic-N, pyrrolic-N and quaternary-N nitrogen atoms entangled with the graphitic structure. Moreover, presence of homogeneous mesopores, hollow nanochannels and nitrogen content found to provide advantages of confinement effect by grafting the Pt nanocatalysts (~2 nm). The Pt@*m*PHCNFs based electrocatalyst exhibited outstanding electrocatalytic activity for ORR and superior long-term operating stability during PEM fuel cell operations.

Results and Discussion

Pt supported on mesoporous, hollow carbon nanofibers were prepared by co-axial electrospinning and thermally induced selective phase separation method. The introduction of mesoporosity and carbonization were performed for based on our previous report [30],[36]. After co-axial electrospinning, the as-spun PAN-$NaHCO_3$/PMMA core-shell nanofibers were stabilized in air at 290 °C for 2 h. During oxidative stabilization, the linear PAN molecules dissociate two hydrogen atoms in the monomeric unit that forms a double bond between the carbon atoms. Meanwhile, the nitrile bond cleaved and transformed into non-meltable cyclic or ladder-like structures, which is the key process responsible for the retention of nanofibrous structure during carbonization. Subsequently, the stabilized nanofibers were carbonized under nitrogen atmosphere at 800 °C for 1 h, wherein the stabilized PAN structure in the shell transformed into graphitic structure with conjugated double bond in the polyaromatic structure. During this process, sacrificial components, such as PMMA from the core and $NaHCO_3$ nanoparticles from shell were decomposed and burnt out, generating the meosporous hollow nanofiber structure in the outer shell. The average size of the mesopores formed in the shell layer was related to the size of the ball milled $NaHCO_3$ nanoparticles (20-50 nm). The formation of carbon nanofibers and the simultaneous removal of $NaHCO_3$ is reported in our previous work[30]. Further, the introduction of oxygen containing functional groups, ie., carboxylic acid groups and hydroxyl groups on the peripheral walls of carbon nanofibers act as effective anchoring sites which can strengthen the interaction of catalyst and carbon support. In order to prepare the stable electrocatalyst, the hydrothermal method was adopted and the whole synthetic strategy for the preparation of Pt/*m*PHCNFs is illustrated in Scheme 1. Upon the introduction of Pt^{2+} ions, the functional groups (C-O-H) present in the peripheral walls of the carbon nanofibers create strong interactions with metal ions (C-O-Pt) through co-ordination or ion exchange reaction[44,45]. The high surface area, mesopores and hollow structure can effectively induce the uniform dispersion of electrocatalysts when it is used as support material. Moreover, it also can provide enormous accessible area for the electrolyte, reactant molecules to contact the supported electrocatalysts (Triple phase boundaries).

The oxidative stabilization process is regarded as an essential step to attain dimensional stability in carbon nanofibers which offers an infusible structure at elevated temperature. The thermal decomposition behavior of the porous carbon nanofibers during stabilization was investigated using DSG and TG analysis (Figure 1a). The initial weight gain was observed in electrospun PAN/$NaHCO_3$nanofibers, which might be due to the absorption of purging gases such as oxygen and nitrogen. As shown in Figure S1, the first weight loss was observed in two temperature ranges around 70-110 °C and 120-150°C which could be due to the loss of water molecules and degradation of methyl methacrylate groups[46]. In addition, PAN-$NaHCO_3$/PMMA nanocomposite nanofibers showed a sharp exothermic DSC peak around 290 °C, which is associated to multiple chemical reactions (dehydrogenation, cross linking and cyclization of nitrile groups) of polyacrylonitrile. The corresponding changes were also evident from the drastic weight loss observed in TG curves. On the other hand, PAN molecules were converted into volatile compounds such as H_2O, HCN, NH_3, CO_2 etc[30,47]. Therefore, 295°C was chosen as the suitable temperature for stabilization process of the core-shell nanofibers.

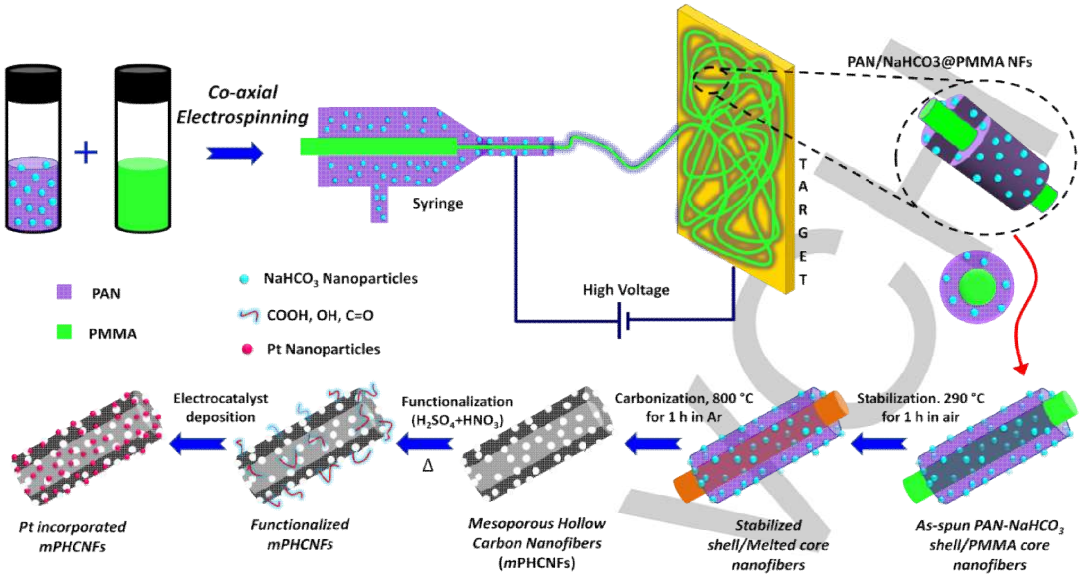

Scheme 1. Schematic diagram illustrating the preparation of Pt/mPHCNFs electrocatalyst, a) coaxial electrospinning of PAN-$NaHCO_3$ shell/PMMA core nanofibers, (b-c) subsequent stabilization and carbonization of the core-shell nanofibers for preparing mesoporous hollow carbon nanofibers, (d) chemical functionalization of mesoporous hollow carbon nanofibers and (e) deposition of Pt nanoparticles on mesoporous hollow carbon nanofiber support materials.

The various stages of the synthesis of PAN-$NaHCO_3$/PMMA based hollow carbon nanofibers were monitored by functional group analysis using ATR-FTIR spectroscopy (Figure 1b). The characteristic stretching vibrations of the electrospun nanofibers appeared at 2243 cm^{-1}, which is ascribed to the presence of nitrile groups (C≡N). The bands located at 1050, 1452, 2932 cm^{-1} correspond to the symmetric and asymmetric vibrations of aliphatic C-H groups (CH and CH_2). The characteristic absorbance peaks at ~1730 cm^{-1} and 1150 cm^{-1} are attributed to the stretching vibrations of C=O and C-O-C confirming the presence PMMA in the nanofibers. Upon stabilization and carbonization processes, the prominent peaks of nitrile groups and aliphatic C-H groups were completely disappeared and revealing the formation of carbon nanofibers. After acidic treatment, the functional groups, such as –OH, –COOH and –SO_3OH were formed on the peripheral walls of the carbon nanofibers. Most importantly, the spectral bands located at 1065 and 925 cm^{-1} corresponds to the stretching and bending vibrations of the –COOH group and a broad peak appeared at ~3450 cm^{-1} was assigned to the O-H stretching frequency of hydroxyl groups. The band appeared at ~1620 cm^{-1} and 1730 cm^{-1} could be assigned to C-O and C=O stretching, respectively. It is worth mentioning that the acidic treatment of *m*PHCNFs provides numerous anchoring sites by means of various functional groups that would contribute in the homogeneous dispersion of Pt nanoparticles.

Raman spectrum is regarded to be a solid method for confirming the carbon phases of the stabilized and carbonized nanofibers of both CNFs and *m*PHCNFs. As shown in Figure 1c, Raman spectrum of the materials exhibited two characteristic broad peaks, approximately centered at 1350 and 1585 cm^{-1} were identified as D-bands corresponding to A_{1g} zone-edge phonon caused by defects or disorder in the graphitic structure and G-bands associated to in-plane tangential stretch vibration mode (E_{2g}) of sp^2 carbon atoms in a hexagonal lattice [48]. The integrated intensity ratio ($R=I_D/I_G$) of the D-band to G-band was calculated to be 0.92 and 0.98, for CNFs and *m*PHCNFs, which reflect the defect formation in carbon lattice of *m*PHCNFs. However, the intensity ratio of *m*PHCNFs was found to be similar to CNFs, indicating the same degree of graphitization.

The microstructure of *m*PHCNFs was investigated by X-ray diffraction (XRD) measurements, as illustrated in Figure 1d. The carbon nanofibers exhibited broad diffraction peaks appeared around 2θ of 25.8° and 45.9 which are indexed to (002) and (101) reflections of carbon. Besides the diffractions of carbon, the Pt/*m*PHCNFs displayed various diffraction peaks located at 2θ values of 39.23°, 45.74°, 67.26°, 80.98° and 85.30° corresponding to (111), (200), (220), (311) and (222) planes which are corroborating the face-centered cubic (fcc) crystal structure (JCPDS card No. 87-0646) of metallic state of platinum. The average crystallite size of Pt nanoparticles was calculated from the Pt (111) peak according to the Scherrer equation, $d= 0.89\lambda/\beta\cos\theta$, where d is the average crystallite size of Pt nanoparticles, λ is the X-ray wavelength (Cu Kα, λ = 0.154 nm), β is the full width at half maximum of (111) peaks in radians and θ is the angle of diffraction [31,49]. The calculated crystallite size of Pt nanoparticles was found to be 2.2 nm for Pt/*m*PHCNFs. The structure and particle size distribution of Pt nanoparticles were further investigated by TEM analysis.

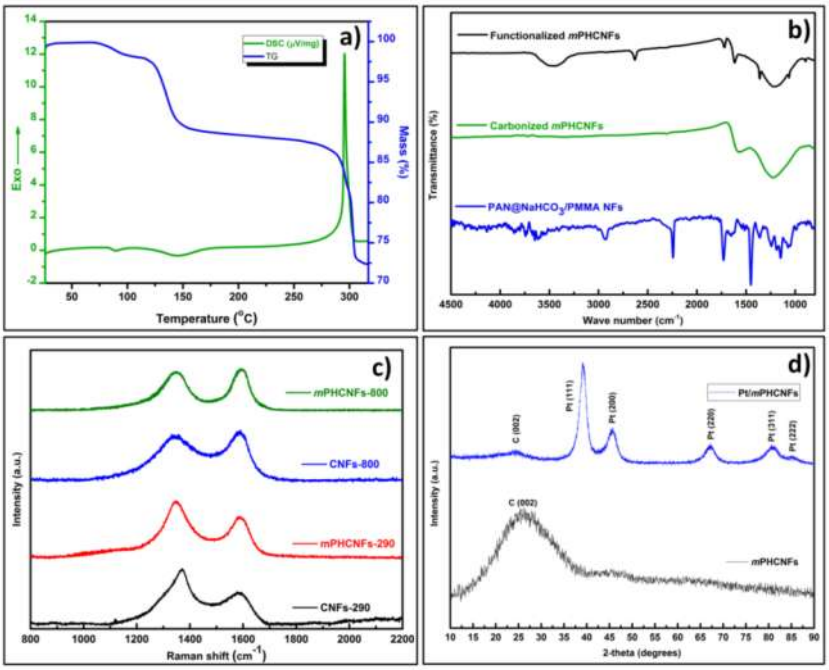

Figure 1. a) DSC/TG thermograms of as-synthesized PAN-$NaHCO_3$/PMMA nanofibers in O_2 atmosphere, b) ATR-FITR spectra of as-synthesized PAN-$NaHCO_3$/PMMA nanofibers, carbonized *m*PHCNFs and functionalized *m*PHCNFs, c) Raman analysis of stabilized and carbonized nanofibers and d) XRD patterns of mesoporous hollow carbon nanofibers and Pt/*m*PHCNFs.

The microstructural and morphological properties of the synthesized materials were further characterized by high resolution transmission electron microscopic (HRTEM) imaging, as shown in Figure 2. Figure 2b shows the continuous fibrous structure of carbon nanofibers having uniform diameter (~200 nm) and smooth surface with tiny micropores (<2 nm). As shown in Figure 2c, the Pt electrocatalyst formed on the surface of the carbon nanofibers are not firmly attached and uniformly distributed leading to the prevalent aggregation of particles. Figure 2d clearly depicts the uniform distribution of numerous identical mesopores and hollow structures along their bodies of *m*PHCNFs with outer wall thickness and core diameters as ~190 and ~50 nm, respectively. The evolution of abundant mesopores in the shell and the hollow structure were mainly due to the complete decomposition of $NaHCO_3$ and PMMA during the carbonization process in the as-spun nanofibers. The diameter of the mesopores in *m*PHCNFs was estimated to be ~20-50 nm, which is corresponding to the pore diameter calculated from nitrogen sorption analysis. Moreover, it is suggested that the combination of abundant mesopores, rough surface and hollow structure in the one dimensional nanofiber structure provide more surface area and active sites for the accommodation, deposition and dispersion of Pt nanoparticles. As evident from Figure 2e, the Pt nanoparticles were found to be homogeneously grafted on mesoporous hollow carbon nanofibers and their average particle size distribution calculated from approximately 200 particles using Image J software was found to be in the range of 2-3 nm. The very small range of particle size could mainly be attributed to the large number of surface functional groups through coordination or ion exchange reaction by forming C-O-Pt from C-O-H groups, which serve as nucleation sites for the growth of Pt nanoparticles[45,50]. More defects produced due to the mesopores and hollow structure created edge nitrogen atoms in carbon lattice and the involvement of nitrogen species in the carbon supports is capable of providing more electron density sites, contributing to homogeneous anchoring of the catalyst nanoparticles due to strong catalyst-support interactions [51]. The pyridinic and pyrrolic N species occupy edge plane sites, which carry extra lone pair of electrons, which strengthen the interactions between electrocatalyst and support and thereby inhibit conglomeration of Pt nanoparticles [7]. Both high-resolution transmission electron microscopic (HRTEM) (Figure 2e) and selected-area electron diffraction (SAED) (inset of Figure 2f) analysis manifests the nanocrystalline nature of Pt nanoparticles. The observed lattice spacing, 0.23 nm is close to the (111) plane of fcc structure of Pt, which is in consistent with the JCPDS database (87-8646). Based on the above observations, it is suggested that the presence of controlled mesopores and hollow structure in the nanofiber can be more favorable for the adsorption and desorption of reactant and product molecules, thereby it also enhances the triple phase boundaries in MEAs.

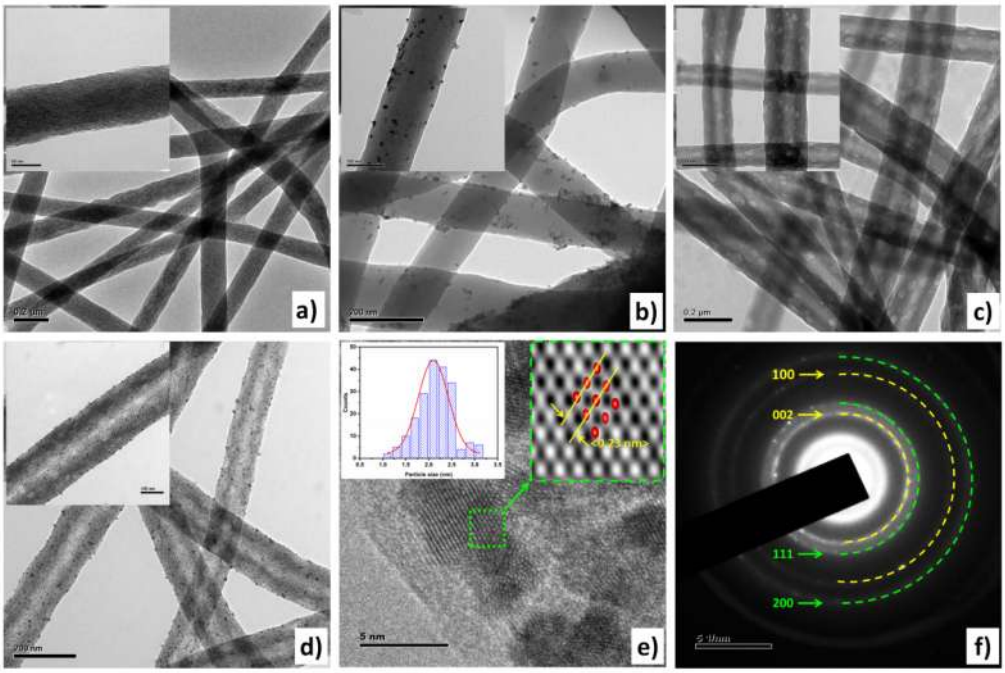

Figure 2. TEM images of (a) pristine CNFs, (b) Pt/CNFs, (c) *m*PHCNFs, (d) Pt/*m*PHCNFs, (e) high resolution image (inset:histogram and plane oriented FFT image) and (f) selected area electron diffraction (SAED) pattern.

The morphologies of CNFs and mPHCNFs were examined by scanning electron microscopy (SEM). Both *m*PHCNFs and CNFs were found to possess long and continuous cylindrical morphologies with homogeneously distributed diameters ranging from 180 to 200 nm. From Figure 3a, it can be seen that the CNFs shows a smooth surface and the cross sectional view indicating the absence of pores. Figure 3b indicates the increase in roughness caused by plenty of mesopores on the outer surface. In addition, the hollow structure ofin the *m*PHCNFs are clearly visible in the cross sectional field-emission SEM image. During thermal decomposition process, hollow core was found to becreated within nanofiber by sacrifical removal of inner PMMA phase and abundant mesopores were formed due to the removal of pore forming agent ($NaHCO_3$ nanoparticles), while the continuous PAN outer phase is easily transformed into carbon.

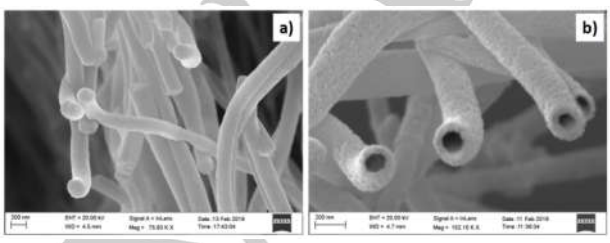

Figure 3. Cross-sectional FESEM images of (a) carbon nanofibers and (b) mesoporous hollow carbon nanofibers.

Undoubtedly, high surface area and suitable porous structure can significantly enhance the catalytic reactions of the electrochemical systems[52]. The surface area characteristics of the prepared CNFs and *m*PHCNFs were evaluated using nitrogen adsorption-desorption isotherms (Figure 4), and the porosities were estimated by non-local density functional theory (NLDFT). The adsorbed quantity of *m*PHCNFs at 0.99 (P/P_o) was about 511Va/cm^3 (STP)/g, while that of CNFs was 167 Va/cm^3(STP)/g. The *m*PHCNFs exhibited a hybrid isotherm of type I and type-IV (monolayer adsorption followed by multilayer adsorption) with a clear H_4-hysteresis loop between the adsorption and desorption branches, as represented in Figure 4. A remarkable nitrogen uptake was observed from the hysteresis loop at an intermediate relative pressure P/P_0 (0.4–0.8) which is due to the characteristic capillary condensation of nitrogen indicative of the generation of slit mesopores (>2 nm) and one at higher relative pressure (0.8–1.0) implying the existence of macropores (2-50 nm), respectively. These observations strongly indicate the formation of mesopores in the shell and hollow structure in the core of *m*PHCNFs *via* the burn-out of $NaHCO_3$ from the shell and PMMA from the core during the carbonization process. Moreover, the pore size distribution (PSD) curves (inset) derived from NLDFT method represent that the pore sizes of *m*PHCNFs and Pt/*m*PHCNFs are in the range of the microporous (< 2 nm) and mesopores zone (2–50 nm), respectively. But, the pore size of the electrocatalyst loaded materials was found to be slightly less compared to pristine carbon nanofibers due to the presence of percolated

nanoparticles into the tiny pores. On the other hand, CNFs based samples depicts the isotherm closed to type-1 and their pore volumes are filled at pressure (P/P_0) below 0.2, which refer to the presence of small micropores (<2 nm). The estimated textural properties of these materials, such as specific surface area (S_{BET}), pore volumes and average pore sizes are summarized in Table 1. From the above observations, it was evident that *m*PHCNFs exhibited superior properties, such as large specific surface area (856 m^2 g^{-1}), high pore volume, controlled size of mesopores and hollow structure which can offer more nucleation sites to improve the electrocatalyst dispersion, smooth diffusion of reactants and electrolyte by providing low resistance pathways for making proper contact between catalyst and electrolyte. Moreover, the electrical conductivity studies of the synthesized materials are shown in Figure S1.

Table 1. Textural characteristics of *m*PHCNFs, PT/*m*PHCNFs, CNFs and PT/CNFs.

Sample	S_{BET}(m^2 g^{-1})[a]	V_{total} (cm^3g^{-1})[b]	V_{meso} (cm^3g^{-1})[c]	V_{micro} (cm^3g^{-1})[d]	APD (nm) [e]
CNFs	150	0.318	0.26	0.06	1.40
Pt/CNFs	143	0.298	0.23	0.06	1.32
*m*PHCNFs	856	0.790	0.44	0.35	22.3
Pt/*m*PHCNFs	780	0.640	0.41	0.23	17.6

[a] S_{BET}-BET surface area. [b] V_{total}- total pore volume. [c] V_{meso}-mesopore volume. [d] V_{micro}-micropore volume. [e] APD- average pore diameter.

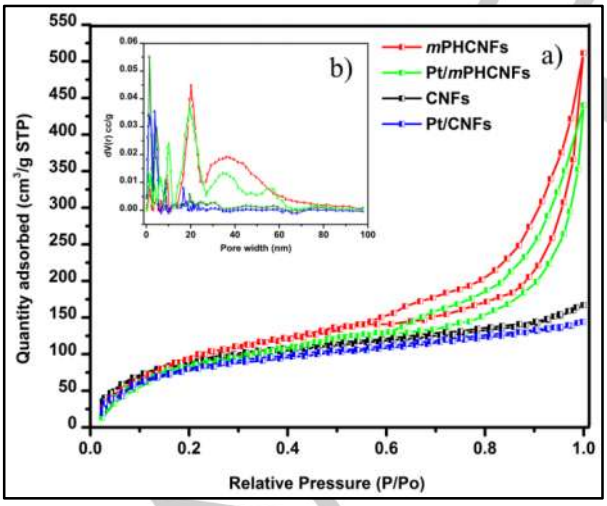

Figure 4. (a) Nitrogen adsorption isotherm curves of *m*PHCNFs, Pt/*m*PHCNFs, CNFs and Pt/CNFs and (b) corresponding pore size distribution (inset).

X-ray photoelectron spectroscopy (XPS) analysis was performed to further investigate the chemical states of nitrogen, platinum, carbon and oxygen species in the synthesized electrocatalyst support materials. The XPS survey spectrum of Pt/*m*PHCNFs is shown in Figure 5a and the calculated percentage of elements are listed in Table 2. C1s spectrum of Pt/*m*PHCNFs shown in Figure 5b can be deconvoluted into four major components with binding energy peaks appearing at 284.8, 285.9, 286.9 and 288.3 eV, which may be respectively attributable to the presence of C=C, C−OH or C-N bond, C=O bond and C=O−O bond. As shown in Figure 5c, the O1s spectra are composed of three individual peaks located at 531.5, 532.8and 534.3eV corresponds to carbonyl, hydroxyl and carboxylic groups, respectively, which are well consistent with the results from C1S spectra. It can be understood from C1s and O1s spectrum that the presence of abundant oxygen-containing functional groups present on the graphitic carbon nanofibers could be more favorable for anchoring and homogeneous dispersion of electrocatalysts [44]. In order to realize the role of nitrogen functionalities towards ORR performance, it is essential to elucidate the types of nitrogen functionalities introduced on the carbon surface. The enlarged spectrum N1s (Figure 5d) can be deconvoluted into four peaks centered at 398.3, 399.8, 400.8, and 402.9 eV indicating the presence of various N species, such as pyridine-like nitrogen atoms (N atom at the edge of hexagonal ring with two adjacent carbon atoms imparting Lewis basicity to the carbon), pyrrolic/pyridine (nitrogen atoms bonded within five-membered heterocyclic ring that contribute to the π system with two *p* electrons), quaternary-N (N bonded to three C atoms within the graphitic basal plane) and pyridinic-N-oxide, respectively. The N atomic ratio calculated from the XPS analysis of Pt/CNFs and Pt/*m*PHCNFs was 3.73 % (Figure S2) and 9.12 %, respectively. The percentages of nitrogen species estimated from the integral areas of the peaks are represented in Figure 5f. Generally, the low Pt loading efficiency was mainly caused by the surface inertness of pristine carbon nanofibers, resulting in less adsorption on carbon nanofibers and easy detachment of Pt nanoparticles during rinsing. But, it has been well demonstrated that the presence of large number of defective sites (pyridinic and pyrrolic nitrogen species at the edge atoms of carbon materials) can form the initial nucleation sites leading to the uniform distribution and smaller size Pt nanoparticles[51,53,54]. The occurrence of more pyridinic and pyrrolic nitrogen species in the mesoporous hollow carbon nanofibers support possessed planer sp^2 hybridization that would not disturb the π-π conjugation in the graphitic structure of carbon nanofibers. Moreover, high electron density and electron donating properties of nitrogen can alter the valance band structure by raising the density of state near to Fermi level leading to reduction of work function that can facilitate the adsorption and reduction of O_2 molecules on the electrocatalyst[55,56]. Figure 5e presents the high resolution Pt 4f spectrum of Pt/*m*PHCNFs originated from the spin orbital coupling of 4f photoelectron transitions, which can be deconvoluted into four individual peaks (two pairs of doublets) at 71.5, 74.9, 72.4, and 76.2 eV.

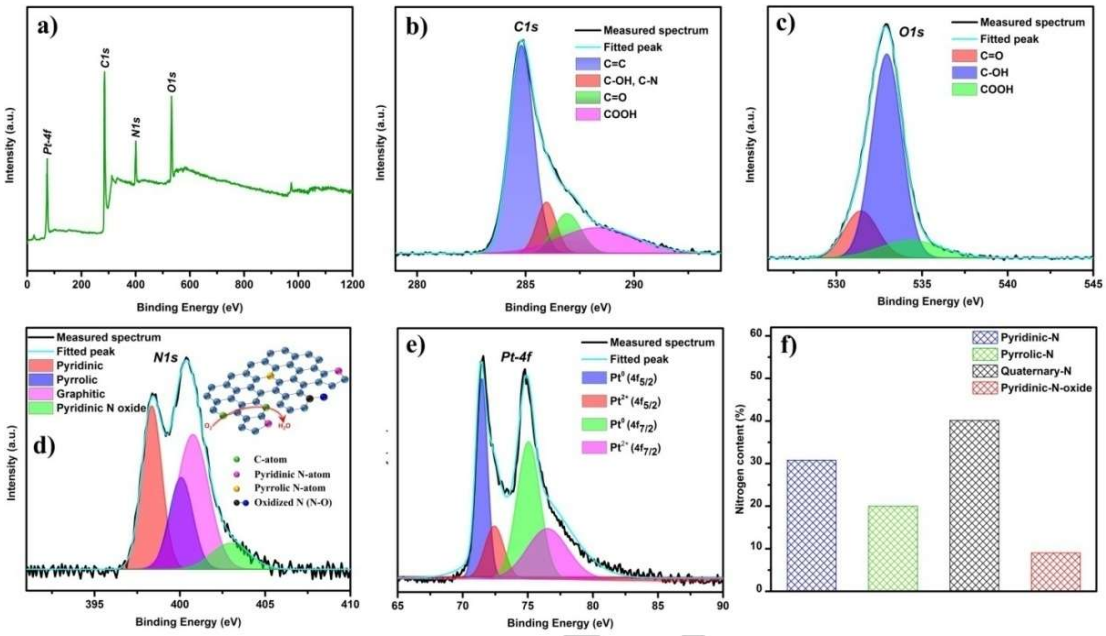

Figure 5.(a) XPS full survey spectrum of Pt/*m*PHCNFs, (b) high-resolution deconvoluted C1speak, c) high-resolution deconvoluted O1s peak, d) High-resolution N1s peak, e) High-resolution Pt4f peak.

The most intense pair peaks with binding energy value of 71.5 and 74.9 eV could be ascribed to metallic Pt 4f7/2 and Pt 4f5/2, whereas the second pair of peaks appeared at 72.4 eV and 76.2 eV are associated with $Pt^{2+}$and Pt^{4+} species. These appearances of Pt^{2+} species (PtO and/or Pt $(OH)_2$) could be resulted from the chemisorptions of oxygen on Pt surface during synthesis. As summarized in Table 2, the area fractions of these Pt and Pt^{2+} peaks were calculated to be 79.7 % and 20.3%, respectively. The integration of peak areas representing that Pt species predominantly exist as metallic phase in Pt/*m*PHCNFs and it is noteworthy that Pt (0) is electrochemically more active than other species.

Table 2. Atomic compositions and N contributions of Pt/*m*PHCNFs electrocatalysts obtained from XPS analysis.

Elemental composition (at %)				Nitrogen content (%)			
C	O	N	Pt	Pyridinic-N (398.3 eV)	Pyrrolic-N (399.8 eV)	Graphitic-N (400.8 eV)	Pyridinic oxide–N (402.9 eV)
71.9	16.4	9.12	2.53	30.8	19.9	40.1	9.2

The mesoporous based carbon nanomaterials showed their strong impact on electrocatalytic performance enhancement towards oxygen reduction reaction. To appraise the electrocatalytic efficiency and stability of Pt/*m*PHCNFs electrocatalysts, CV and LSV measurements were performed under nitrogen purged and oxygen purged acidic medium and their results were compared with that of Pt/CNFs and Pt/C. Figure 6a shows the typical cyclic voltammograms of various electrocatalysts using N_2 saturated H_2SO_4 (0.5 M) over a scan range of 0 to 1.2 V with a scan rate of 50 mV/s. A pair of strong hydrogen adsorption and desorption on Pt surface was clearly observed in both cathodic and anodic region between 0 and 0.4 V for Pt/*m*PHCNFs which was comparatively larger than other two electrocatalysts. The determination electrochemically active surface areas (ECSAs) from hydrogen adsorption/desorption regions were considered to be significant parameter to evaluate the intrinsic electrocatalytic activity of platinum based catalysts. The ECSAs of Pt nanoparticles was calculated by measuring the areas under the hydrogen adsorption–desorption peaks after correcting the double layer current according to the following equation [44],

$$ECSA = Q_H/(210 \times M_{Pt}) \quad \text{..... (1)}$$

Where, Q_H is the charge exchange during hydrogen desorption, 210 μC/cm^2 is the electrical charge for monolayer adsorption of hydrogen atom on bright Pt, M_{Pt} represents the mass of Pt loaded on the working electrode. Table 3 summarizes the charge exchange from hydrogen desorption, content of platinum (M_{Pt}) and calculated electrochemical surface area of Pt/*m*PHCNFs, Pt/CNFs and Pt/C.

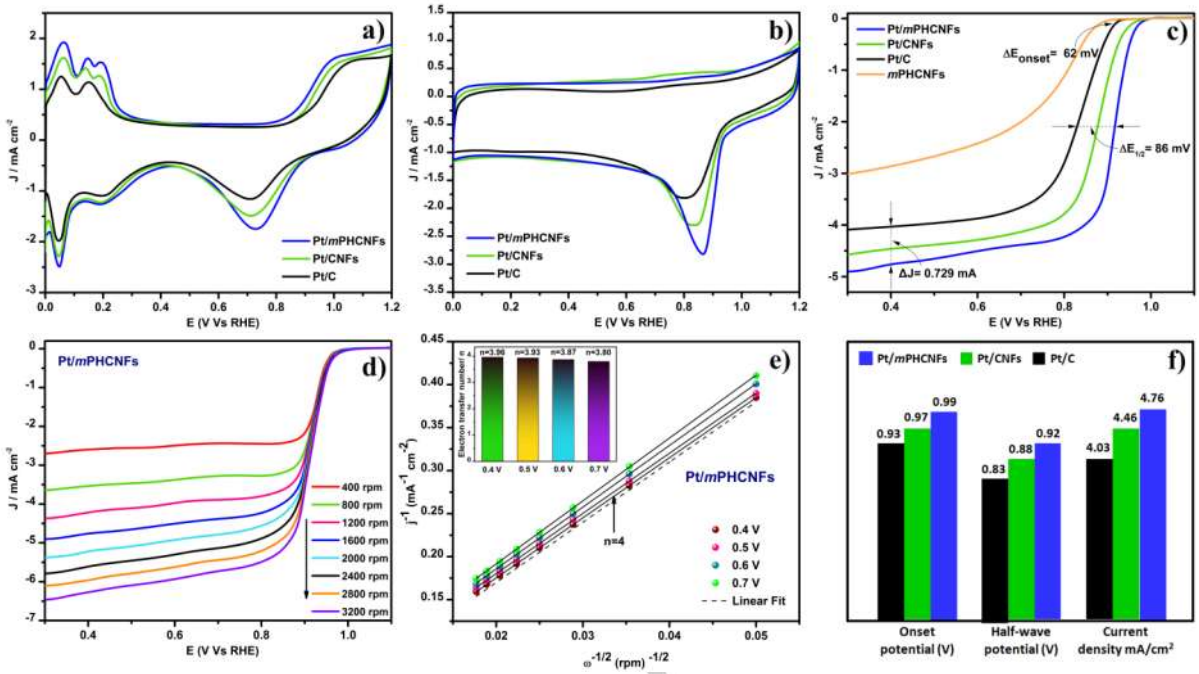

Figure 6. Electrocatalytic activity studies of Pt/*m*PHCNFs, Pt/CNFs and Pt/C in 0.5 M H_2SO_4. (a) Cyclic voltammograms of Pt/*m*PHCNFs, Pt/CNFs and Pt/C in N_2 purged electrolyte at 50 mV/s (b) Cyclic voltammograms of Pt/*m*PHCNFs, Pt/CNFs and Pt/C in O_2 purged electrolyte at 50 mV/s, (c) linear sweep voltammetry curves of Pt/*m*PHCNFs, Pt/CNFs, *m*PHCNFs and Pt/C using rotating disc electrode (1600 rpm) in O_2 purged electrolyte at 10 mV/s, (d) linear sweep voltammetry curves of Pt/*m*PHCNFs, Pt/CNFs and Pt/C at various rotation rates (400-3200 rpm), (e) Koutecky-Levich (K-L) plot, (f) Comparison of electrocatalytic performance of various electrocatalysts obtained from LSV results.

The ECSAs for Pt/*m*PHCNFs were calculated as 98.8 m^2/g^{-1} which is much higher than that of Pt/CNFs (62.1 m^2/g^{-1}) and commercial Pt/C (48.9 m^2/g^{-1}). It is inferred that the Pt/*m*PHCNFs based electrocatalyst exhibited outstanding electrochemical activity that could be mainly attributed to the smaller and uniformly grafted Pt nanoparticles, high ratio of metallic Pt(0) content and nitrogen defects that provided more intrinsic active sites. Moreover, the presence of mesopores and hollow structure in the one dimensional carbon nanofibers support are more favorable for proton to access these electrocatalyst regions, where as more number of Pt nanoparticles in CNFs and Vulcan carbon will be buried in tiny micropores that hinders the ability of protons to access these regions

Table 3. Summary of electrochemical parameters calculated from CV of Pt/CNFs, Pt/*m*PHCNFs and Pt/C in 0.5 M H_2SO_4.

Sample	Q_H (μC)	M_{Pt} (mg)	ECSA (m^2/g)
Pt/*m*PHCNFs	410.8	0.0198	98.8
Pt/CNFs	246.4	0.0189	62.1
Pt/C	200.2	0.0195	48.9

Q_H, total charge acquired from hydrogen desorption curve. M_{Pt}, the amount of Pt loading on working electrode. ECSA, electrochemical surface area.

In order to evaluate the ORR performance of prepared electrocatalysts, cyclic voltammetry was conducted in O_2-saturated H_2SO_4 electrolyte at a scan rate of 50 mV/s. Figure 6b showed a well defined single cathodic peak observed at 0.87, 0.83, 0.81 V for Pt/*m*PHCNFs, Pt/CNFs and Pt/C respectively, which imply the superior activity of Pt/mPHCNFs towards oxygen reduction reaction. In general, ORR in acidic medium is a complicated multistep process which includes two main electrochemical pathways, (i) Four electron reduction pathway wherein oxygen directly converts into water (equation 1) and (ii) two electron reduction pathway with two electrons for oxygen into hydrogen peroxide as an intermediate product and then reduced to water (equation 2-3). The four electron transfer is considered as more desirable pathway for fuel cell reactions [44].

$$O_2 + 4H^+ + 4e^- \rightarrow H_2O \text{ (Four electron)} \quad (1)$$

$$O_2 + 2H^+ + 2e^- \rightarrow H_2O_2 \text{ (Two electron)} \quad (2)$$

$$H_2O_2 + 2H^+ + 2e^- \rightarrow 2H_2O \quad (3)$$

Linear sweep voltammetry (LSV) was performed to gain further insight into ORR activity of synthesized Pt/*m*PHCNFs electrocatalyst using rotating disk electrode (RDE) at 1600 rpm with sweeping rate of 10 mV/s. Figure 6c, demonstrates the polarization plots of various electrocatalysts such as, Pt/*m*PHCNFs, Pt/CNFs and Pt/C. A characteristic set of

polarization curves of Pt/*m*PHCNFs showed two distinguishable potential regions, well defined diffusion-limiting current region (0 to 0.80 V), followed by a mixed kinetic-diffusion control region (0.80 to 0.95 V). The performance of oxygen reduction reaction is mainly related to its onset potential, half-wave potential and limiting current density obtained from their RDE polarization curve. The onset potential and half wave potential for Pt/*m*PHCNFs (998 and 917 mV) are highly positive than that of Pt/CNFs (0.97 and 0.88) and commercial Pt/C (935 and 831 mV) electrocatalysts. The observed limiting current densities of the catalysts at 0.4 V are represented in the order of Pt/*m*PHCNFs (4.76 mA cm^{-2}) >Pt/CNFs (4.46 mA cm^{-2}) >Pt/C (4.03 mA cm^{-2}). The electrochemical parameters are summarized in Table 4. An outstanding ORR electrocatalytic activity of Pt/*m*PHCNFs is probably because of the excellent characteristics, such as uniform distribution and strong interaction of small size Pt nanoparticles, suitable mesopores, hollow structure, and synergistic catalysis effect of N-C. On the other hand, it is inferred that the contrast results observed in Pt/CNFs and Pt/C was mainly due to the presence of high ratio micropore volume that are not large enough to effectively facilitate the transportation of reactant and product molecules during ORR.

Table 4. Electrochemical parameters derived from CV and LSV measurements.

Electrocatalyst	Onset potential (mV)	Limited current $density_2$ mA/cm (at 0.4 V)	Half wave potential (mV)
Pt/*m*PHCNFs	998	4.76	917
Pt/CNFs	974	4.46	878
Pt/C	935	4.03	831

Linear sweep voltammetry curves of Pt/*m*PHCNFs were obtained at various rotation rates (400-3200 rpm) using RDE technique to further investigate the electrocatalytic mechanism of ORR. As shown in Figure 6d, the limiting current density for the oxygen reduction reaction proportionally increases as the rotational velocity of the electrode increases. The kinetic parameters at different rotation speeds was carefully evaluated based on the following Koutecky-Levich (K-L) equation 4 and 5, the slopes of the best linear fit lines were used to calculate the electron transfer number (n) per oxygen molecule in the ORR process[36].

$$\frac{1}{J} = \frac{1}{J_k} + \frac{1}{J_d} = -\frac{1}{nFkC_{O_2}^b} - \frac{1}{0.62nFD_{O_2}^{2/3}\nu^{-1/6}C_{O_2}^b\omega^{1/2}} \quad (4)$$

$$B = 0.62nFC_{O_2}(D_{O_2})^{2/3}\nu^{-1/6} \quad (5)$$

Where j_k and j_d are the kinetic and diffusion limiting current densities, n is the transferred electron number per oxygen molecule involved in the reduction at electrodes, F is the Faraday constant (96486 C mol^{-1}), k is the electron transfer rate constant, D_{O2} is the diffusion coefficient of oxygen in H_2SO_4 (1.8 x 10^{-5} cm^2 s^{-1}), C_{O2} is the bulk concentration of O_{2in} H_2SO_4 (1.1 x 10^{-6} mol cm^{-3}), υ is the kinematic viscosity of the electrolyte (0.01 cm^2 s^{-1}), ω is the angular velocity ($\omega = 2\pi N$, where N is the linear rotation speed).

In order to explore the kinetic aspects of oxygen reduction reaction for Pt/*m*PHCNFs electrocatalysts, Koutecky–Levich plots of 1/j vs. $1/\omega^{1/2}$ are plotted in Figure 6e at various fixed potentials. The K–L plots clearly display linear lines that are very parallel to the theoretical line based on four electron transfer, which indicates the first-order ORR kinetics with respect to dissolved oxygen. The electron transfer numbers for ORR were calculated from the slope of the Koutecky–Levich plots at the fixed potentials of 0.4 V, 0.5 V, 0.6 V and 0.7 V vs. RHE. As shown in Figure 6e (inset), the calculated n values for Pt/*m*PHCNFs are close to 4 for the whole range of potentials studied, which indicates that the reduction of oxygen predominantly proceeded through a direct four-electron reduction pathway. Therefore, the highest near four electron pathway implied that Pt/*m*PHCNFs had excellent electrochemical activity with a first order reaction kinetics as compared to other two electrocatalysts. Based on these results, it can be suggested that Pt-based catalysts using mesoporous, hollow carbon nanofibers as support material possess excellent electrocatalytic activity for ORR due to the high amount of Pt-loading, uniform Pt distribution and suitable pore texture. In addition, the large amount of mesopores can provide low resistance pathways and shorter diffusion routes for electrolyte ions. Moreover, nitrogen containing carbon support material can exhibit good catalytic activity for oxygen reduction reaction. The electron accepting tendency of nitrogen atoms in the Pt/*m*PHCNFs creates a net positive charge on adjacent carbon atoms that readily accept electrons from the anode for facilitating the ORR.

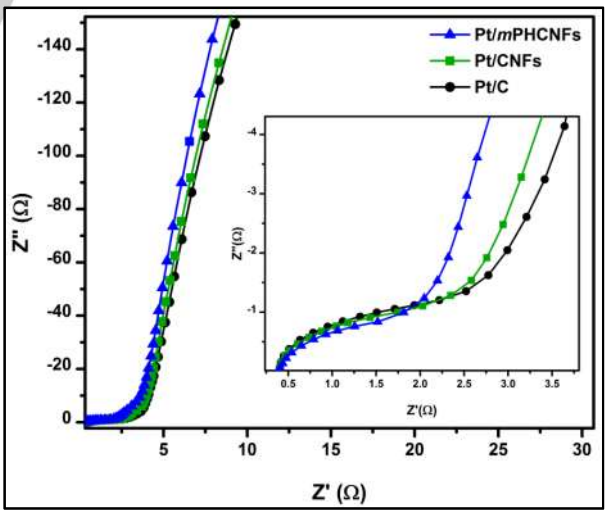

Figure 7. Nyquist plots of Pt/*m*PHCNFs, Pt/CNFs and Pt/C cathodes obtained by electrochemical impedance spectroscopy in the range of 100 kHz to 10 MHz (inset: magnified 0.25-4.0Ω region)

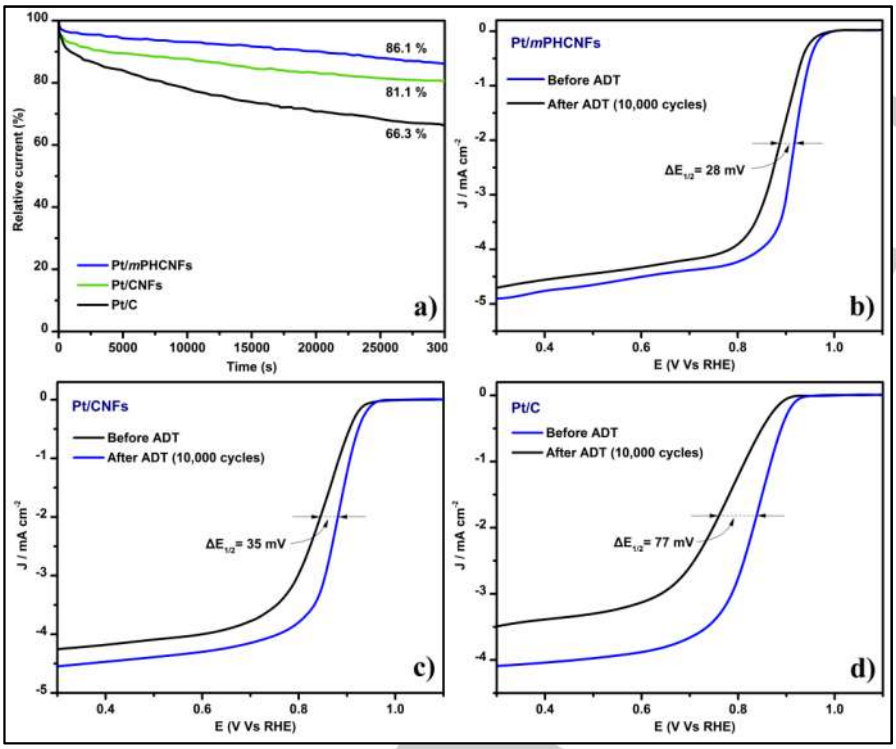

Figure 8. (a) Chronoamperometric response current-time (j-t) of the Pt/*m*PHCNFs, Pt/CNFs and Pt/C for 30,000 s in O_2-saturated 0.5 M H_2SO_4 at a constant potential of 0.6 V, ORR polarization curves (1600 rpm) of (b) Pt/*m*PHCNFs, (c) Pt/CNFs and (d) Pt/C before and after acceleration durability test (10,000 cycles) in O_2-saturated 0.5 M H_2SO_4 at a scan rate of 10 mV/s.

Electrochemical impedance spectroscopy is a powerful technique that provides critical information related to the internal resistance of electrode material and resistance between electrode-electrolyte interfaces. The complex-plane impedance plots (Nyquist plots) of various electrodes such as, Pt/*m*PHCNFs, Pt/CNFs and Pt/C were obtained using a three electrode cell at the open circuit voltages as depicted in Figure 7. Generally, the Nyquist plot can be mainly divided into three regions; (1) nearly vertical straight line to the realistic impedance axis at low frequency region associated with the diffusive resistance of the electrolyte in the porous structure, (2) a semi-circle at high frequency region related to the estimation of charge transfer resistance (R_{ct}), which is related to the surface properties of porous electrode and (3) the slope of the 45^o portion in the low frequency region of the Nyquist plots corresponds to Warburg resistance (R_w), which is associated with the frequency dependent ion diffusion in the electrolyte/electrode interface. It is well known that a small semicircle obtained at high frequency region reflects the smaller charge transfer resistance [57–59]. The diameter of the semi circle of Pt/*m*PHCNFs was found to be smaller as compared to other two electrocatalysts which imply significant decrease in charge transfer resistance at the electrode/electrolyte interface. In the low frequency region, the straight line of Pt/*m*PHCNFs was more vertical than those of other two electrocatalysts and this phenomenon implies low diffusion resistance of electrolyte ions and enhanced adsorption/desorption of ion on the surface of the electrode. On the basis Nyquist plots, the estimated charge transfer resistance for the Pt/*m*PHCNFs (1.5 Ω) was found to be very less as compared to Pt/CNFs (2.4 Ω) and Pt/C (2.9 Ω). Hence, from the above discussions, it can be clearly understood that high electronic conductivity and good accessibility of ion to the Pt/*m*PHCNFs electrode material could be more advantageous for achieving superior electrochemical performance. Altogether we postulate that the overall electrochemical performance enhancement could be attributed to several aspects, (i) The amalgamation of the high specific surface area, suitable pore size, hollow structure and large mesopore volumes provides the charge transport and shortest path way for ion diffusion, (2) the uniform distribution of small size catalyst nanoparticle on one dimensional conducting carbon nanofibers contributing in the efficient transport of electron across the graphitic layer (3) optimum level of nitrogen content offers a significant electrocatalytic activity and acts towards ORR process.

Long-term durability is regarded to be the most crucial factor in fuel cell technology, Figure 8a represents the current-time (j-t) chronoamperometric curves of Pt/*m*PHCNFs, Pt/C and Pt/C obtained from acceleration durability test performed in 0.5 M H_2OS_4 at 0.6 V . It is clearly observed that the CA curves of all other electrocatalyst, except Pt/*m*PHCNFs declined with

increasing time which is due to the decrease of electrocatalytic activity after long time operation. Significantly, the current density of Pt/*m*PHCNFs was retaining 86.1 % over 30,000 s, while Pt/CNFs (81.1 %) and Pt/C (66.3 %) displays a fast decline in current density. Accelerated degradation testing (ADT) also was carried out by performing linear sweep voltammetry with 10,000 potential cycles in oxygen saturated acidic electrolyte at a scan rate of 10 mV s^{-1}. Pt/*m*PHCNFs (Figure 8b) exhibited only minimal loss (28 mV) in half wave potential after 10,000 potential cycles, indicating its better durability. Meanwhile, the Pt/CNFs and Pt/C demonstrate poor stability by means of their half wave potential difference of 35 and 77 mV, respectively. The improved electrochemical stability of Pt/*m*PHCNFs was mainly due to the unique structure which is abundant mesopores pores, hollow structure, rough surface and pyridinic/pyrrolic nitrogen sites present in the graphitic layers that strongly affix the Pt nanoparticles which prevent them from detachment and conglomeration during long operative conditions.

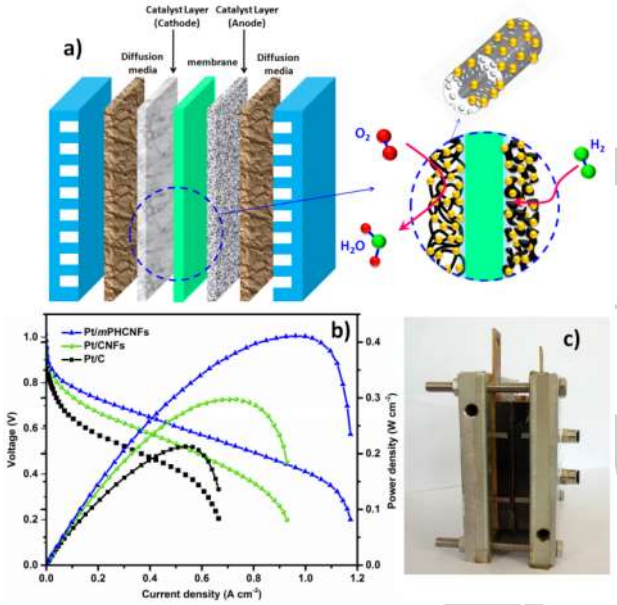

Figure 9. (a) Schematic illustration of the various components in PEMFCs (H_2-O_2), (b)single cell polarization curves of the Pt/*m*PHCNFs, Pt/CNFs and commercial Pt/C cathodes with a Pt loading of 0.3 mg/cm^2 and the anode catalyst was 20 % commercial Vulcan Pt/C, (c) assembly of single cell with the fabricated MEA.

The performance of membrane electrode assembly (MEA) in an H_2-O_2 fuel cell may differ from the half cell measurements and these evaluations using single cell testing can provide deeper insight into the practical applicability[14]. Figure 9 illustrated the polarization curves (v-j and p-j) of PEMFC electrodes with various electrocatalysts, such as Pt/*m*PHCNFs, Pt/CNFs and Pt/C on the cathode and commercial Pt/C as the anode electrocatalysts. Under standard conditions, the reversible potential of the electrochemical reaction in PEMFC is 1.23 V, but the actual voltage can slightly change during operative condition of the fuel cell that may be due to three types of irreversible losses (activation, ohmic and concentration polarization losses).

Table 5. Polarization curve parameters from single cell performance test.

Cathode electrocatalysts	OCV (mV)	J_{max} (mA.cm^{-2})	P_{max} (mW.cm^{-2})	Current density (j) at P_{max}(mA.cm^{-2})
Pt/*m*PHCNFs	1016	1173.5	411.4	961.2
Pt/CNFs	979	928.1	297.4	732.2
Pt/C	939	664.7	212.8	537.2

It should be emphasized that the Pt/*m*PHCNFs showed highest open circuit voltage (OCV) of about 1.02 V, while Pt/CNFs and Pt/C showed an OCV of 0.98 V and 0.94 V, respectively. The Pt/*m*PHCNFs based cathode electrocatalyst exhibited highest peak power density (411.4 mW/cm^2) which exceeds that of carbon nanofiber and commercial Pt based PEMFCs. The maximum current density delivered by the Pt/*m*PHCNFs electrocatalyst was 1174 mA/cm^2, which corresponds to an enhancement of 21 % compared with Pt/CNFs (928 mA/cm^2) and 69 % compared with that of commercial Pt/C (665 mA/cm^2) electrocatalysts under the same testing conditions. Moreover, it is obvious that the performance of Pt/*m*PHCNFs based MEA is better in higher and lower current density regions which imply the minimal losses in activation, ohmic and concentration polarization region. The obtained polarization results are summarized in Table 5. These results revealed that the excellent performance of Pt/*m*PHCNFs was probably due to a high electrochemically active surface area of the electrocatalyst (improved electrode-electrolyte contact) and a controlled size of mesoporous and hollow structure in the one dimensional carbon nanofibers (better electron conduction and favorable mass transport).

Conclusions

To summarize, hierarchical mesoporous hollow carbon nanofibers were successfully prepared through simple coaxial electrospinning method and thermally induced selective phase separation mechanism. Pt/*m*PHCNFs were further tailored with Pt electrocatalyst and its electrocatalytic properties were investigated for PEM fuel cell applications. Strongly grafted metallic Pt nanoparticles formed on the hollow mesoporous carbon nanofibers were found to be small and well-distributed, owing to the confinement effects of pyridinic/pyrrolic nitrogen content, mesoporous structure and hollow nanochannels. The Pt/*m*PHCNFs based electrocatalyst support materials preserved unique combination of mesopores/hollow structure, high surface area (780 m^2g^{-1}), large pore volume and high nitrogen content in 1D nanofibrous structure. The superior electrocatalytic activity

and stability towards ORR is predominantly associated with the formation of enhanced triple phase boundaries because of the small and homogeneous distribution of nanoparticles, the enrichment of pyridinic and pyrrolic nitrogen content, easy accessibility of O_2 molecules and ions in the catalytic sites due to the mesopores and hollow structure. The Pt/*m*PHCNFs based PEMFC has demonstrated excellent performance with a power density of 411.4 mW cm^{-2}. Therefore, the investigation suggest that the developed novel mesoporous hollow carbon nanofiber based electrocatalyst support material can be a propitious replacement of conventional carbon support used for the oxygen reduction reaction in PEMFCs.

Experimental Section

Materials and Methods

Polyacrylonitrile (PAN, Mw = 150,000, Aldrich) was used as the carbon shell material and ball milled sodium bicarbonate ($NaHCO_3$, 99.9%, Merck) nanoparticles was used as a pore forming agent in the shell. Poly methyl methacrylate (PMMA, Mw = 120,000, Aldrich) was used as a sacrificial core component for creating the hollow structure. N, N-dimethylformamide (DMF, Merck) was used to prepare the core and shell polymer solutions. Hexachloroplatinic acid ($H_2PtCl_6.6H_2O$, Aldrich), ethylene glycol (EG, Merck), sulphuric acid (H_2SO_4, Merck) and nitric acid (HNO_3, Merck) were used to prepare Pt/*m*PHCNFs electrocatalyst. The commercial electrocatalyst Vulcan XC-72 (20 wt % Pt/C, Cabot Corp.), carbon papers (Toray), Nafion® 117 membrane and 5% Nafion® 117 solution (Dupont Industries) were used for the fabrication of membrane electrode assembly. All materials were used as-received without any further purification.

Synthesis of PAN-$NaHCO_3$@PMMA Core-Shell nanofibers by Co-axial Electrospinning

Mesoporous hollow carbon nanofibers were synthesized from a stable suspension of PAN-$NaHCO_3$ blend which was used as the shell material while the PMMA was used as a sacrificial core polymer feed solution during coaxial electrospinning. The outer shell fluid was prepared by dispersing ball-milled $NaHCO_3$ (1% wt/v) nanoparticles with PAN/DMF (7%wt/v) solution for 2 h at 60 °C and ultrasonicated for 30 min to form a homogeneous blend mixture of PAN-$NaHCO_3$. The inner core fluid was prepared by dissolving PMMA in DMF (12 wt/v %) by stirring for 2 h at 60 °C. The resultant fluids were utilized for electrospinning and were inhaled through two separate 10 mL syringes. The spinneret consisted of two stainless-steel blunt tip needles with diameters of 18-gauge (outer) and 21-gauge (inner) installed coaxially as core and shell respectively. The two feed solutions prepared as above were fed using a syringe pump (World precision instruments Inc, USA, SP200I) with a constant flow rate (0.6 ml/hr). A high voltage power supply (Glassman High Voltage Inc., USA, EH30P3) was used for electrospinning and the constant voltage of 30 kV was applied between the needle and grounded copper foil (10x10 cm). The distance between the capillary tip and the collector plate was fixed as 30 cm. All experiments were conducted under ambient conditions.

Fabrication of mesoporous hollow carbon nanofibers

The electrospun co-axial nanofibers were stabilized at 290 °C in a horizontal tubular furnace under air atmosphere for 2 h and subsequently heated at 800 °C in nitrogen atmosphere for 1 h to carbonize the PAN. A gradual progressive heating rate (5 °C/min) was applied for the stabilization and carbonization process. During carbonization process, a continuous flow of nitrogen gas was supplied in order to expel the volatile by-products without creating any structural defects. In order to remove the impurities from the carbon nanofibers, the obtained nanofiber mats were immersed in 1 M HCl and rinsed thoroughly with deionized water and ethanol. The functionalization of the samples was carried out under refluxed condition using solution mixture of H_2SO_4 (3 M) and HNO_3 (3M) (3:1 v/v) at 120 °C for 8 h. After the surface treatment, the resultant hollow carbon nanofibers were separated, washed thoroughly with deionized water and dried in a vacuum oven at 120 °C for 6 h [44,60].

Preparation of Pt nanoparticles supported on *m*PHCNFs

Pt nanocatalysts (~20 wt. %) were deposited on the mesoporous hollow carbon nanofibers (Pt/*m*PHCNFs) by ethylene glycol reduction through hydrothermal method[29,48,61,62]. Briefly, 40 mg of synthesized hollow porous carbon nanofibers based support material was soaked in 20 mL of ethylene glycol. Calculated amount of $H_2PtCl_6.H_2O$ was slowly added into this suspension and pH was adjusted to 13.0 by adding NaOH (2.5 M) solution. The solution was transferred into 50 mL Teflon-lined autoclave and heated at 120 °C for 4 h. Finally, the product was separated from the solution, washed with deionized water for several times and dried in vacuum oven at 100 °C. Similarly, the carbon nanofiber based electrocatalyst material also was prepared adopting the same method for comparison and samples were labelled as Pt/*m*PHCNFs and Pt/CNFs. The Pt content was determined using inductively coupled plasma atomic emission spectroscopy (ICP-AES). The Pt loading for Pt/*m*PHCNFs, Pt/CNFs and Pt/C were estimated to be 19.82 wt%, 18.93 wt% and 19.51 wt%, respectively.

Characterization

The thermal properties of electrospun fibers were analyzed by TG/DSC in the heating range of 30-320 °C at 5 °C/min heating rate using NETZSCH (Jupiter STA449F3, Germany). X-ray diffraction patterns (XRD) of the samples were aquired using a Panalytical X-pert X-ray diffractometer equipped with Cu-Ka radiation (λ=1.5406 Å) source at a generator voltage of 40 kV and a generator current of 30 mA with a scanning speed of 5° min^{-1} from 2θ angles ranging 5° to 90°. The microstructural parameters were determined using JCPDS software. Raman spectra were recorded with a Horiba Jobin spectrometer (LabRAM HR) at an excitation laser beam wavelength of 514 nm. Fourier transform infrared (FT-IR) spectroscopic measurement was performed on a ATR-FTIR (Shimadzu, IR affinity-1) spectrometer with a scan range of 400-4000 cm^{-1} in order to understand the molecular structural changes of the nanofibers during stabilization, carbonization and functionalization process. The hollow tubular structure, porous fiber morphology, crystalline behavior, dispersion and particle size of Pt nanoparticles were examined by high-resolution transmission electron microscope (HRTEM) (JEOL JEM 2100, Japan). The prepared samples were deposited on a carbon film supported by a 200-mesh copper grid, operated at 200 kV. Textural properties of carbon nanofibers were estimated using Brunauer−Emmett−Teller (BET) method by nitrogen adsorption-desorption isotherms at 77 K. The measurements were carried out using an Autosorb-1 apparatus (Quantachrome, USA). Prior to the measurements, the nanofibers were degassed under vacuum at 573 K for 8 h.,. The surface area, total pore volume, average pore diameter and pore-size distributions of the materials were determined using BET plot and non-local density functional theory (NLDFT) method. X-ray photoelectron spectroscopy (XPS) analysis was conducted using a Thermoscientific instrument equipped with Al Kα (hu = 1486.6 eV) as the

X-ray radiation source. Elemental chemical ratios of the samples were calculated from the integral areas of XPS peaks.

Electrochemical measurements

The electrochemical performance and stability measurements of the samples were investigated using cyclic voltammetry (CV), linear sweep voltammetry (LSV), chronoamperometry (CA) and electrochemical impedance spectroscopy (EIS) on electrochemical work station (CH instruments (CHI600E, USA)) in 0.5 M H_2SO_4. The experiments were conducted by employing a conventional three-electrode system with a polished glassy carbon (GC) working electrode (geometrical area: 0.0706 cm^2) and GC RDE (geometric area: 0.3848 cm^2) for CV and LSV studies, respectively. A Pt wire and Ag/AgCl (sat. KCl) were served as a counter electrode and reference electrode (all the potentials were reported in this study are with respect to reversible hydrogen electrode (RHE), respectively. GC electrode was cleaned by polishing with 0.3 and 0.05 µm alumina slurries in order to achieve a mirror finish, subsequently washed and ultrasonicated with water and acetone. The working electrode was prepared by a Nafion bonded films (20 % Pt/*m*PHCNFs and Pt/CNFs). The Pt loaded porous hollow carbon nanofibers were fabricated on the glassy carbon electrode by using 0.1% solution of Nafion and the coating was further dried at room temperature in order to maintain nanofiberous structure. Similarly, CNFs and commercial catalysts (20 wt% Pt/C (Vulcan XC-72)/ethanol/Nafion mixture) also were investigated for comparison. Pt/C ink was prepared by mixing 2 mg of 20 wt % Pt/C commercial electrocatalyst with1 mL of 0.25 wt% Nafion/ethanol mixture, followed by ultrasonication for 30 min. The slurry (20µL) of Pt/C ink was applied onto a clean GC electrode surface and slowly dried in air. The overall loading of Pt catalyst applied on glassy carbon electrode was about ~ 21 µg Pt cm^{-2}. In order to acquire reproducible and reliable results, freshly prepared electrolyte (0.5 M H_2SO_4) was used for each measurements. High pure nitrogen and oxygen were bubbled through the electrolyte solution for 30 min to create nitrogen and oxygen atmosphere near to the working electrode.

PEMFC single cell fabrication

In order to fabricate a cathode layer, a slurry of the electrocatalyst prepared from the mixture of required amount of Pt/*m*PHCNFs, Nafion® ionomer solution (5 wt%), isopropanol and deionized water. The slurry was magnetically stirred for 30 min and subjected to ultra-sonication for 30 min. The homogeneous slurry was spray coated on the hydrophobic gas diffusion layer (carbon paper pre-treated with 30 % PTFE solution) and dried in air oven at 80 °C for 30 min. Similarly, the anode was prepared using commercial Pt/C (20 wt%). After being dried, the anode and cathode layers (5x5 cm^2 active areas) were hot pressed with a Nafion® 117 membrane (DuPont Inc.) at 130 °C and 10 MPa for 10 min in order to fabricate a membrane electrode assembly (MEA). A single cell was assembled using the fabricated MEA and flow channel machined graphite plates, which was further used to evaluate the performance of the electrocatalysts. Pt loading in the case of both anode and cathode was maintained to be 0.1 and 0.3 mg/cm^2, respectively. Hydrogen (400 mL/min) and oxygen (200 mL/min) with a 40 % relative humidity were supplied to the anode and cathode, respectively. The back pressure was not maintained during the cell testing. The experimental conditions such as, cell temperature, pressure were maintained to be 40 °C and 3 bar, respectively. The single cell polarization performance was evaluated using a fuel cell test station (Biologic FCT-50S, France).

Acknowledgements

We gratefully acknowledge the support of PSG Institute of Advanced Studies, Coimbatore, India, for carrying out this work. The authors also acknowledge DST-SERB (Ref: SB/S3/CE/038/2015) for financial support.

Keywords: mesoporous hollow carbon nanofibers • electrocatalyst support • triple phase boundaries • oxygen reduction • fuel cells

[1] C. Chen, C. Luo, X. Zhang, Y. Li, J. Huang, B. Chen, J. Chen, *New J. Chem. New J. Chem* **2017**, *41*, 7432.

[2] A. Brouzgou, S. Q. Song, P. Tsiakaras, *Appl. Catal. B Environ.* **2012**, *127*, 371.

[3] W. Zhang, P. Sherrell, A. I. Minett, J. M. Razal, J. Chen, *Energy Environ. Sci.* **2010**, *3*, 1286.

[4] H. Nan, D. Dang, X. L. Tian, *J. Mater. Chem. A* **2018**, *6*, 6065.

[5] I. Kone, A. Xie, Y. Tang, Y. Chen, J. Liu, Y. Chen, Y. Sun, X. Yang, P. Wan, *ACS Appl. Mater. Interfaces* **2017**, *9*, 20963.

[6] X. L. Tian, Y. Y. Xu, W. Zhang, T. Wu, B. Y. Xia, X. Wang, *ACS Energy Lett.* **2017**, *2*, 2035.

[7] X. X. Wang, Z. H. Tan, M. Zeng, J. N. Wang, *Sci. Rep.* **2015**, *4*, 4437.

[8] J. Tang, J. Liu, N. L. Torad, T. Kimura, Y. Yamauchi, *Nano Today* **2014**, *9*, 305.

[9] Y. Nie, L. Li, Z. Wei, *Chem. Soc. Rev.* **2015**, *44*, 2168.

[10] S. M. Unni, S. Ramadas, R. Illathvalappil, S. N. Bhange, S. Kurungot, *J. Mater. Chem. A* **2015**, *3*, 4361.

[11] L. Castanheira, W. O. Silva, F. H. B. Lima, A. Crisci, L. Dubau, F. Maillard, *ACS Catal.* **2015**, *5*, 2184.

[12] S. Shahgaldi, J. Hamelin, *Carbon N. Y.* **2015**, *94*, 705.

[13] F. Alcaide, G. Álvarez, O. Miguel, M. J. Lázaro, R. Moliner, A. López-Cudero, J. Solla-Gullón, E. Herrero, A. Aldaz, *Electrochem. commun.* **2009**, *11*, 1081.

[14] A. M. Zainoodin, S. K. Kamarudin, M. S. Masdar, W. R. W. Daud, A. B. Mohamad, J. Sahari, *Appl. Energy* **2014**, *113*, 946.

[15] F. A. Viva, M. M. Bruno, E. A. Franceschini, Y. R. J. Thomas, G. Ramos Sanchez, O. Solorza-Feria, H. R. Corti, *Int. J. Hydrogen Energy* **2014**, *39*, 8821.

[16] T. Soboleva, K. Malek, Z. Xie, T. Navessin, S. Holdcroft, *ACS Appl. Mater. Interfaces* **2011**, *3*, 1827.

[17] D. Dru, S. Baranton, J. Bigarré, P. Buvat, C. Coutanceau, *ACS Catal.* **2016**, *6*, 6993.

[18] S. Martin, Q. Li, J. O. Jensen, *J. Power Sources* **2015**, *293*, 51.

[19] Y. Su, H. Liu, Z. Yan, M. Feng, J. Tang, H. Du, *Electrochim. Acta* **2015**, *164*, 182.

[20] S. N. Stamatin, M. Borghei, R. Dhiman, S. Ma, V. Ruiz, E. Kauppinen, E. M. Skou, *"Applied Catal. B, Environ.* **2015**, *162*, 289.

[21] X. Tang, Z. Xie, Q. Huang, G. Chen, M. Hou, B. Yi, *Nanoscale* **2015**, *7*, 7971.

[22] E. Lohrasbi, M. Javanbakht, S. A. Mozaffari, *Ind. Eng. Chem. Res.* **2016**, *55*, 9154.

[23] G.-P. Kim, M. Lee, Y. J. Lee, S. Bae, H. D. Song, I. K. Song, J. Yi, *Electrochim. Acta* **2016**, *193*, 137.

[24] H. Liang, W. Wei, Z. Wu, X. Feng, K. Müllen, *J. Am. Chem. Soc.*

2013, *135*, 16002.
[25] J. Sanetuntikul, T. Hang, S. Shanmugam, *Chem. Commun.* **2014**, *50*, 9473.
[26] N. Mansor, A. B. Jorge, F. Corà, C. Gibbs, R. Jervis, P. F. McMillan, X. Wang, D. J. L. Brett, *J. Phys. Chem. C* **2014**, *118*, 6831.
[27] J. Kim, Y.-S. Chun, S.-K. Lee, D.-S. Lim, *RSC Adv.* **2015**, *5*, 1103.
[28] M. Ghasemi, S. Shahgaldi, M. Ismail, B. H. Kim, Z. Yaakob, W. R. Wan Daud, *Int. J. Hydrogen Energy* **2011**, *36*, 13746.
[29] R. Padmavathi, D. Sangeetha, *Electrochim. Acta* **2013**, *112*, 1.
[30] K. K. Karthikeyan, P. Biji, *Microporous Mesoporous Mater.* **2016**, *224*, 372.
[31] D.-S. Yang, S. Chaudhari, K. P. Rajesh, J.-S. Yu, *ChemCatChem* **2014**, n/a.
[32] G. Ren, X. Lu, Y. Li, Y. Zhu, L. Dai, L. Jiang, *ACS Appl. Mater. Interfaces* **2016**, *8*, 4118.
[33] K. K. Karuppanan, A. V. Raghu, M. K. Panthalingal, S. Ramanathan, T. Kumaresan, B. Pullithadathil, *J. Mater. Chem. A* **2018**, *4*, 10986.
[34] Y. Wang, J. Jin, S. Yang, G. Li, J. Jiang, *Int. J. Hydrogen Energy* **2016**, *41*, 11174.
[35] W. Xu, S. Tao, *J. Mater. Chem. A Mater. energy Sustain.* **2016**, *4*, 16272.
[36] K. K. Karuppanan, A. V. Raghu, M. K. Panthalingal, S. Ramanathan, T. Kumaresan, B. Pullithadathil, *J. Mater. Chem. A* **2018**, *6*, 12768.
[37] W. Zhang, Z. Y. Wu, H. L. Jiang, S. H. Yu, *J. Am. Chem. Soc.* **2014**, *136*, 14385.
[38] Q. Shi, Y. Lei, Y. Wang, H. Wang, L. Jiang, H. Yuan, D. Fang, B. Wang, N. Wu, Y. Gou, *Curr. Appl. Phys.* **2015**, *15*, 1606.
[39] Z. Liu, D. Fu, F. Liu, G. Han, C. Liu, Y. Chang, Y. Xiao, M. Li, S. Li, *Carbon N. Y.* **2014**, *70*, 295.
[40] A. G. El-Deen, N. A. M. Barakat, K. A. Khalil, H. Y. Kim, *New J. Chem.* **2014**, *38*, 198.
[41] B.-S. Lee, S.-B. Son, K.-M. Park, W.-R. Yu, K.-H. Oh, S.-H. Lee, *J. Power Sources* **2012**, *199*, 53.
[42] S. Hong, S. Lee, U. Paik, *Electrochim. Acta* **2014**, *141*, 39.
[43] B.-S. Lee, S. Son, K. Park, G. Lee, K. H. Oh, S. Lee, W. Yu, *ACS Appl. Mater. Interfaces* **2012**, *4*, 6702.
[44] R. S. Zhong, Y. H. Qin, D. F. Niu, X. S. Zhang, X. G. Zhou, S. G. Sun, W. K. Yuan, *Electrochim. Acta* **2013**, *89*, 157.
[45] L. Ren, Y. Xing, *Electrochim. Acta* **2008**, *53*, 5563.
[46] A. Mittal, R. Ahmad, I. Hasan, *Desalin. Water Treat.* **2016**, *57*, 19820.
[47] L. Huang, J. Cheng, G. Qu, X. Li, Y. Hu, W. Ni, D. Yuan, Y. Zhang, B. Wang, *RSC Adv.* **2015**, *5*, 23749.
[48] J. J. Shao, Z. J. Li, C. Zhang, L. F. Zhang, Q. H. Yang, *J. Mater. Chem. A* **2014**, *2*, 1940.
[49] A. V. Raghu, K. K. Karuppanan, B. Pullithadathil, *ACS Sensors* **2018**, *3*, 1811.
[50] A. J. Plomp, D. S. Su, K. P. De Jong, J. H. Bitter, *J. Phys. Chem. C* **2009**, *113*, 9865.
[51] B. Yue, Y. Ma, H. Tao, L. Yu, G. Jian, X. Wang, X. Wang, Y. Lu, Z. Hu, *J. Mater. Chem.* **2008**, *18*, 1747.
[52] X. L. Tian, L. Wang, B. Chi, Y. Xu, S. Zaman, K. Qi, H. Liu, S. Liao, B. Y. Xia, *ACS Catal.* **2018**, *8*, 8970.
[53] P. Roy, R. Soc, J. I. Met, W. Vernon, E. Akeroyd, J. Desmaison, M. Billy, C. R. A. Sci, S. Dominique, B. Devillers, J. Bardoll, M. Froman, R. Bell, C. Roy, **1997**.
[54] Z. Li, Q. Gao, H. Zhang, W. Tian, Y. Tan, W. Qian, Z. Liu, *Sci. Rep.* **2017**, *7*, 43352.
[55] B. P. Vinayan, R. Nagar, N. Rajalakshmi, S. Ramaprabhu, *Adv. Funct. Mater.* **2012**, *22*, 3519.
[56] D. He, Y. Jiang, H. Lv, M. Pan, S. Mu, *Appl. Catal. B Environ.* **2013**, *132–133*, 379.
[57] Z. Liu, D. Fu, F. Liu, G. Han, C. Liu, Y. Chang, Y. Xiao, M. Li, S. Li, *Carbon N. Y.* **2014**, *70*, 295.
[58] C. R. Bradbury, J. Zhao, D. J. Fermín, *J. Phys. Chem. C* **2008**, *112*, 10153.
[59] K. Wang, Q. Meng, Y. Zhang, Z. Wei, M. Miao, *Adv. Mater.* **2013**, *25*, 1494.
[60] K. Rajavel, M. Lalitha, J. K. Radhakrishnan, L. Senthilkumar, R. T. Rajendra Kumar, *ACS Appl. Mater. Interfaces* **2015**, *7*, 23857.
[61] X. Zhang, N. Hao, X. Dong, S. Chen, Z. Zhou, Y. Zhang, K. Wang, *RSC Adv.* **2016**, *6*, 69973.
[62] S. Zhang, Z. Wen, K. Rui, C. Shen, Y. Lu, J. Yang, *J. Mater. Chem. A* **2015**, *3*, 2568.

Entry for the Table of Contents

ARTICLE

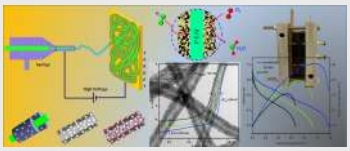

A novel mesoporous hollow carbon nanofibers is developed as a support material for high performance and durable PEM fuel cells.

*Karthikeyan K Karuppanan,[a] Appu V Raghu[a], Manoj Kumar Panthalingal[b] and Biji Pullithadathil[a,c]**

Page No. – Page No.

Title

Tailored Hollow Core/Mesoporous Shell Carbon Nanofibers as Highly Efficient and Durable Cathode Catalyst Supports for Polymer Electrolyte Fuel Cells.